

# Novel mechanical behavior of ZnO nanorods

J. Wang<sup>a</sup>, A.J. Kulkarni<sup>b</sup>, F.J. Ke<sup>a,c</sup>, Y.L. Bai<sup>c</sup>, M. Zhou<sup>a,b,\*</sup>

<sup>a</sup> Department of Physics, Beihang University, Beijing 100083, China

<sup>b</sup> G.W.W. School of Mechanical Engineering, Georgia Institute of Technology, Atlanta, GA 30332-0405, USA

<sup>c</sup> Institute of Mechanics, Chinese Academy of Sciences, Beijing 100080, China

Received 22 July 2007; received in revised form 11 October 2007; accepted 25 October 2007

Available online 1 November 2007

## Abstract

A novel stress–strain relation with two stages of linear elastic deformation is observed in [0001]-oriented ZnO nanorods under uniaxial tensile loading. This phenomenon results from a phase transformation from wurtzite (WZ,  $P6_3mc$  space group) to a body-centered tetragonal structure with four-atom rings (denoted as BCT-4) belonging to the  $P4_2/mnm$  space group. The analysis here focuses on the effects of nanorod size and temperature on the phase transformation and the associated mechanical behavior. It is found that as size is increased from 19.5 to 45.5 Å, the critical stress for nucleation of the transformation decreases by 25% from 21.90 to 16.50 GPa and the elastic moduli of the WZ- and BCT-4-structured nanorods decrease by 24% (from 299.49 to 227.51 GPa) and 38% (from 269.29 to 166.86 GPa), respectively. A significant temperature effect is also observed, with the critical stress for transformation initiation decreasing 87.8% from 17.89 to 2.19 GPa as temperature increases from 300 to 1500 K.

© 2007 Elsevier B.V. All rights reserved.

**Keywords:** Phase transformation; ZnO nanorods; Molecular dynamics

## 1. Introduction

Nanomaterials made of metals such as gold, silver, copper and semiconductors such as zinc oxide (ZnO), gallium nitride (GaN) and tin dioxide (SnO<sub>2</sub>) have been fabricated in recent years [1–5]. Among these materials, ZnO is highly versatile because of its inherent semiconductivity and piezoelectricity which exist even in bulk form and exciting attributes such as size dependence of properties, pseudoelasticity and thermo-mechanical coupling at the nanoscale [6–11]. Because of this reason, ZnO nanostructures are potential components for nanodevices which exploit these novel attributes. In particular, ZnO nanorods and nanobelts have already found applications in ultra-sensitive sensors for detecting chemical and biological species, nanoresonators, nanocantilevers, field effect transistors and nanogenerators [12–16].

Integration of these nanostructures in systems requires an understanding of their behavior, properties, and functionalities. In this paper, we set out to characterize the tensile behavior of hexagonal nanorods with the [0001] growth orientation, six {0110} lateral crystalline surfaces and lateral dimensions of 19.5–45.5 Å [17,18]. Three stages of deformation are observed, including elastic stretching of the WZ phase, structural transformation to a body-centered-tetragonal with four-atom rings (BCT-4) structure and elastic stretching of the BCT-4 structure following the transformation. First principles calculations previously reported show that this transformation is indeed energetically favorable and the transformed structure corresponds to a distinct minimum on the enthalpy surfaces of ZnO under conditions of the uniaxial tensile stress considered [19]. Crystallographic characteristics of the BCT-4 structure and the transformation process leading to this previously unknown structure are analyzed here. The size and temperature dependence of the transformation and the mechanical behavior of the nanorods are also analyzed. In particular, the variations of the critical stress for transformation

\* Corresponding author. Address: G.W.W. School of Mechanical Engineering, Georgia Institute of Technology, Atlanta, GA 30332-0405, USA. Tel.: +1 404 894 3294; fax: +1 404 894 0186.

E-mail address: [min.zhou@gatech.edu](mailto:min.zhou@gatech.edu) (M. Zhou).

initiation, transformation strains, residual strains upon unloading, the elastic moduli and the ultimate tensile strength are quantified.

## 2. Computational framework

The ZnO nanorods have hexagonal cross-sections and are wurtzite-structured single crystals with a sixfold symmetry around the [0001] axis and six {0110} lateral crystalline surfaces, as illustrated in Fig. 1. The lattice constants for the wurtzite structure are  $a = 3.249 \text{ \AA}$ ,  $u = 0.3862 \text{ \AA}$  and  $c = 5.206 \text{ \AA}$  [18]. Here,  $u = uc/c$  denotes the relative offset between the Zn and O basal planes along the [0001] orientation (see Fig. 1). The nanorod is generated by repeating a unit wurtzite cell along the [0001], [0110] and [2110] directions. Periodic boundary conditions are used along the axial direction with a computational cell length of  $145.8 \text{ \AA}$ . To study the size effect, five lateral dimensions ( $d = 19.5, 26.0, 32.5, 39.0$  and  $45.5 \text{ \AA}$ ) are considered. The minimum lateral dimension analyzed here is chosen such that it is larger than the shortest cutoff radius ( $r = 8.7 \text{ \AA}$ ) of the interatomic potential employed [6,20]. The analyses are carried out at five temperatures (300, 600, 900, 1200 and 1500 K) to quantify the effect of temperature on the behavior.

Molecular dynamics (MD) simulations [21] using a Buckingham-type interatomic potential are carried out [6,20]. The calculations use Newton's second law

$$\mathbf{f}_i = m_i \ddot{\mathbf{r}}_i \quad (1)$$

for each atom to determine the atomic positions and velocities at finite system temperatures. Here  $\mathbf{f}_i$  is the force on atom  $i$ , and  $m_i$  and  $\ddot{\mathbf{r}}_i$  are the mass and acceleration of atom  $i$ . The equations of motion are integrated using a leapfrog verlet (LV) scheme to yield the velocities ( $\mathbf{v}_i$ ) and positions

( $\mathbf{r}_i$ ). The LV scheme proceeds by advancing the atomic velocities at half timestep ( $t + \Delta t/2$ ) through

$$\mathbf{v}_i \left( t + \frac{\Delta t}{2} \right) = \mathbf{v}_i \left( t - \frac{\Delta t}{2} \right) + \Delta t \frac{\mathbf{f}_i}{m_i}. \quad (2)$$

The atomic positions are then advanced through

$$\mathbf{r}_i(t + \Delta t) = \mathbf{r}_i(t) + \Delta t \mathbf{v}_i \left( t + \frac{\Delta t}{2} \right). \quad (3)$$

In all cases considered here, a timestep of  $\Delta t = 1 \text{ fs}$  is used.

The forces on atoms are calculated from the gradient of the potential energy ( $\mathbf{f}_i = -\partial U / \partial \mathbf{r}_i$ ) where the potential energy is expressed as  $U = \sum_{i=1}^N \sum_{j=1, j \neq i}^N u(r_{ij})$ . Here,  $u(r_{ij})$  is the pairwise interaction energy determined from the Buckingham-type interatomic potential in the form of

$$u(r_{ij}) = \frac{q_i q_j}{4\pi\epsilon_0 r_{ij}} + A \exp\left(\frac{-r_{ij}}{\rho}\right) - \frac{C}{r_{ij}^6}. \quad (4)$$

In the above expression,  $r_{ij}$  is the distance between two atoms,  $q_i$  is the charge on ion  $i$  and  $A$ ,  $\rho$  and  $C$  are potential parameters. The first term in Eq. (4) considers long-range Coulomb interactions due to electric charges and the second and third terms model short-range interactions. Parameters  $A$ ,  $\rho$  and  $C$  are fitted to the structure and properties of ZnO using classical and quantum mechanical methods [6]. The potential has been shown to accurately predict the equilibrium lattice energy, cell parameters, elastic and dielectric constants for all the existing polymorphs of bulk ZnO. Extensive perfect lattice, defect and monovalent ion incorporation simulations have been successfully carried out using this potential [6,20,22]. The potential also effectively predict surface properties such as surface energies [6]. This is especially important in the simulations of nanowires and nanorods whose high surface-to-volume ratios are known to significantly affect behavior.

To obtain the free-standing configurations of the nanorods, pre-loading relaxations are carried out at desired temperatures without external loading until thermodynamic quantities (such as energy, stress, and temperature) indicate that statistical steady states have been reached. The relaxations require up to 8 ps using the NPT algorithm of Melchionna et al. [23,24]. This algorithm couples the EOM with a Nosé–Hoover thermostat and barostat. For isotropic fluctuations of the simulation cell, the EOM are written as [25]:

$$\begin{aligned} \frac{d\mathbf{r}_i(t)}{dt} &= \mathbf{v}_i(t) + \eta(t)[\mathbf{r}_i(t) - \mathbf{R}_0], \\ \frac{d\mathbf{v}_i(t)}{dt} &= \frac{\mathbf{f}_i(t)}{m_i} - [\chi(t) + \eta(t)]\mathbf{v}_i(t), \\ \frac{d\chi(t)}{dt} &= \frac{N_t k_B}{Q} [T(t) - T_{\text{ext}}] + \frac{1}{Q} \left\{ W[\eta(t)]^2 - k_B T_{\text{ext}} \right\}, \\ \frac{d\eta(t)}{dt} &= \frac{3}{W} V(t) [P(t) - P_{\text{ext}}] - \chi(t)\eta(t), \\ \frac{dV(t)}{dt} &= 3\eta(t)V(t), \end{aligned} \quad (5)$$

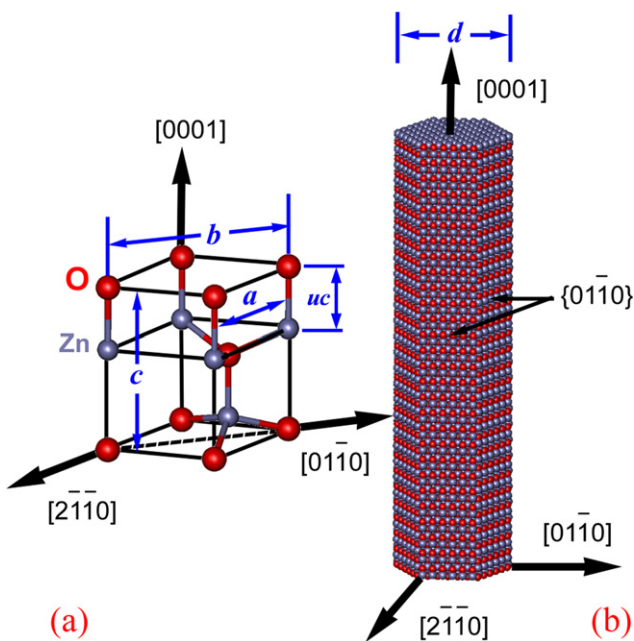


Fig. 1. (a) Lattice structure of wurtzite ZnO and (b) configuration of a [0001]-oriented ZnO nanorod with a lateral dimension ( $d$ ) of  $32.5 \text{ \AA}$ .

where  $\mathbf{R}_0$  is the system center of mass,  $N_f$  is the number of degrees of freedom,  $V$  is the system volume,  $\chi$  and  $\eta$  are the thermostat and barostat friction coefficients respectively,  $T$  is the instantaneous temperature, and  $T_{\text{ext}}$  is the specified temperature.  $P$  and  $P_{\text{ext}}$  are the instantaneous and specified values of pressure, respectively.  $Q = N_f k_B T_{\text{ext}} \tau_T^2$  and  $W = N_f k_B T_{\text{ext}} \tau_P^2$  are the effective masses of the thermostat and barostat, respectively.  $\tau_T$  and  $\tau_P$  denote the specified constants for temperature and pressure fluctuations, respectively.

Following the initial relaxations, a quasi-static loading scheme is employed to effect tensile deformation and to obtain the mechanical response of the nanorods. Approximation to quasi-static tensile loading in each deformation increment is achieved in two steps. First, stretching at a strain rate of 0.005/ps is carried out for 0.5 ps using a modified version of the NPT algorithm of Melchionna et al. [23,24]. The modification to the EOM embodied in Eq. (5) includes a specification of the evolution equation of  $\eta$  through the addition of a damping coefficient ( $\gamma$ ) to subside the fluctuations in pressure. This evolution equation is

$$\frac{d\eta(t)}{dt} = \frac{3}{W} V(t) [P(t) - P_{\text{ext}}] - \gamma \eta(t). \quad (6)$$

Following the NPT algorithm for loading, the axial strain is held constant and the nanorod is relaxed for 3 ps via an algorithm for NVT ensemble [21] at the specified temperature. The algorithm for the NVT ensemble uses the Nosé–Hoover thermostat and the modified equations of motion in form of

$$\begin{aligned} \frac{d\mathbf{r}_i(t)}{dt} &= \mathbf{v}_i(t), \\ \frac{d\mathbf{v}_i(t)}{dt} &= \frac{\mathbf{f}_i(t)}{m_i} - [\chi(t)]\mathbf{v}_i(t), \\ \frac{d\chi(t)}{dt} &= \frac{N_f k_B}{Q} [T(t) - T_{\text{ext}}]. \end{aligned} \quad (7)$$

Unloading is implemented in a similar manner with a reduction in strain for each unloading step. Each loading or unloading deformation increment results in a nominal strain change of 0.25%. The virial formula as modified by Zhou [26] is used to calculate the stress. In the virial stress definition, the average stress over a volume  $\Omega$  around a particle  $i$  at position  $\mathbf{r}_i$  is

$$\sigma = \frac{1}{\Omega} \left( -m_i \mathbf{v}_i \otimes \mathbf{v}_i + \frac{1}{2} \sum_{j(\neq i)} \mathbf{r}_{ij} \otimes \mathbf{f}_{ij} \right). \quad (8)$$

Zhou [26] demonstrated that the mechanical force term  $\frac{1}{2\Omega} \sum_{j(\neq i)} \mathbf{r}_{ij} \otimes \mathbf{f}_{ij}$  alone is a valid stress measure. This stress definition is independent of the kinetic energy or mass transfer and can be identified with the Cauchy stress. In the cases considered here, the kinetic energy term in Eq. (8) is found to be very small relative to the mechanical force term. The Young's modulus is calculated as the slope of the relevant linear stage of the stress–strain curve.

### 3. Results and discussion

The pre-loading relaxation results in reconstructions of the  $\{01\bar{1}0\}$  side facets of the nanorods.  $\{01\bar{1}0\}$  crystalline planes in bulk ZnO consist of rows of Zn–O dimers aligned in the  $[0001]$  orientation. These dimers are bonded to dimers in the neighboring layer and this geometric construction repeats indefinitely, resulting in a coordination number of 4 for each atom. In the nanorods, however, the coordination number of the surface dimers is lower, as a result of the reduced number of neighboring atoms. The lower coordination corresponds to higher lattice energies which provide a driving force for surface reconstruction to lower the energy of the system. The relaxed structures with lower energies are achieved by an in-plane expansion of the surface layers and an increase in the inter-layer distances between the outermost surface layers. Similar surface reconstructions have also been observed through experiments and density functional theory (DFT) calculations of the surface structures of ZnO [27].

#### 3.1. WZ $\rightarrow$ BCT-4 transformation

Fig. 2 shows the stress–strain response of a 32.5 Å nanorod. Three distinct stages (A  $\rightarrow$  B, B  $\rightarrow$  C and C  $\rightarrow$  D) are observed. The first stage (A  $\rightarrow$  B) corresponds to the elastic stretching of the WZ structure up to a strain of 7.4%. Further deformation leads to a precipitous stress drop (B  $\rightarrow$  C) which results from a structural transformation into a body-centered-tetragonal lattice with four-atom rings (BCT-4) (see Fig. 3a). This WZ to BCT-4 transformation occurs through a combination of (1) the breaking of one half of the Zn–O bonds on  $\{01\bar{1}0\}$  planes along the  $[0001]$  direction (A in Fig. 3b) and (2) the formation of an equal number of Zn–O bonds along the same direction (B in Fig. 3b) next to the broken bonds. This process repeats on alternate planes along the  $[01\bar{1}0]$  direction.

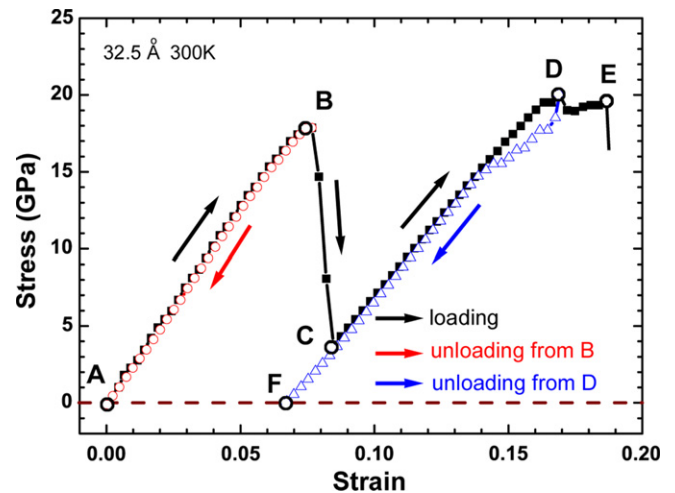


Fig. 2. Stress–strain relation under uniaxial tensile loading and unloading of a 32.5 Å nanorod at 300 K.

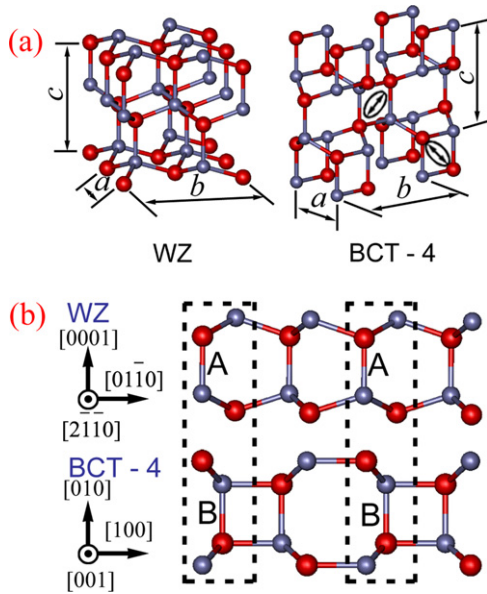


Fig. 3. (a) Wurtzite (WZ) and newly discovered BCT-4 structures and (b) crystallographic transition between the WZ and the BCT-4 structures through breaking and formation of bonds.

Crystallographic analysis reveals that the transformed phase consists of four-atom ( $2Zn$  and  $2O$ ) rings arranged in a BCT lattice (Fig. 3a). The 4-atom ring at the center

Table 1  
Lattice constants of stress-free WZ and BCT-4 structures

	$a$ (Å)	$b$ (Å)	$c$ (Å)	$b/a$	$c/a$
WZ [Point A, Fig. 2]	3.25	5.65	5.20	1.73	1.60
BCT-4 [Point F, Fig. 2]	3.26	5.66	5.52	1.74	1.69
BCT-4 [Point C, Fig. 2]	3.25	5.63	5.63	1.73	1.73

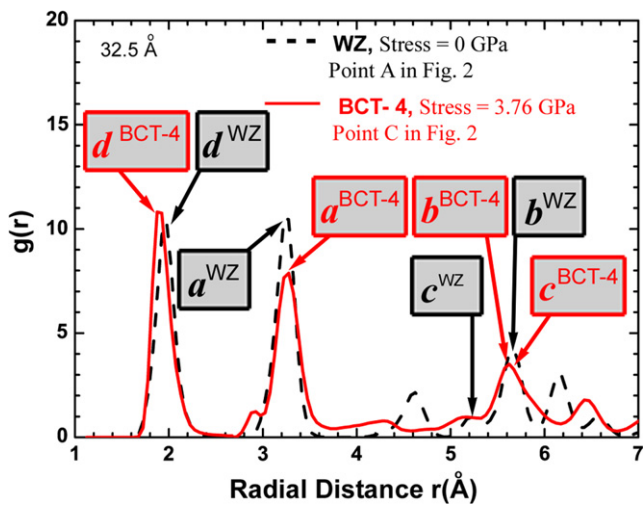


Fig. 4. Radial distribution function (RDF) profiles for a 32.5 Å WZ-structured nanorod before loading (point A in Fig. 3, dash line) and upon completion of structure transformation to BCT-4 (point C in Fig. 3, solid line).

has an orientation different (rotated by  $90^\circ$ ) from that of the rings at the corners of the tetragonal lattice cell. Fig. 3a also shows the lattice parameters  $a$ ,  $b$  and  $c$  for the WZ and BCT-4 structures. Their respective values at

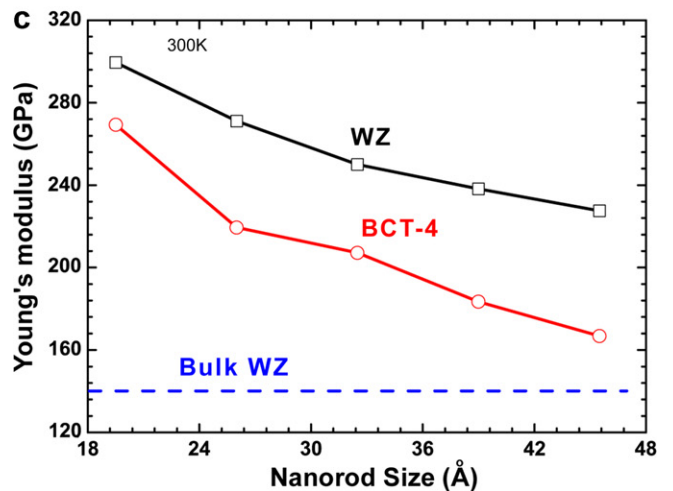
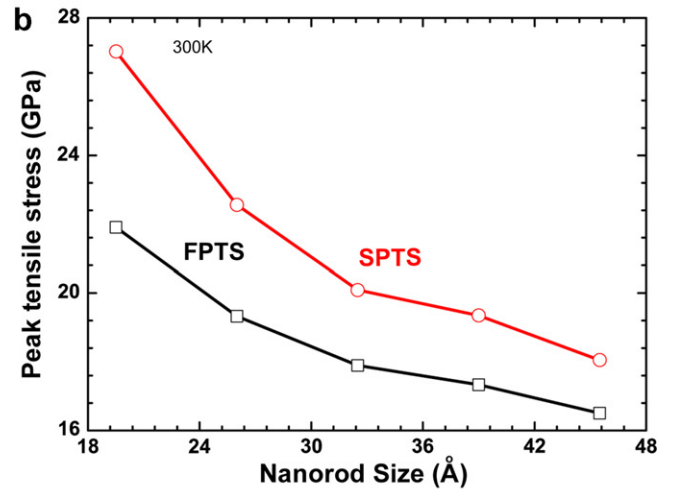
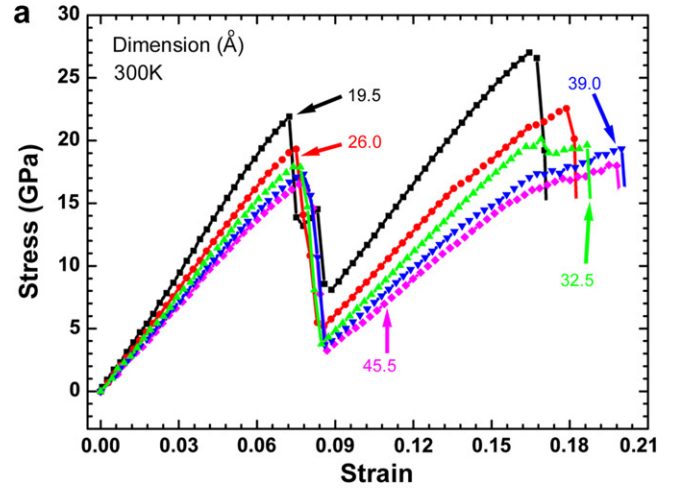


Fig. 5. Size dependence of elastic responses, (a) Stress–strain relations, (b) critical stress for transformation nucleation (FPTS) and failure strength (SPTS) and (c) elastic moduli of WZ and BCT-4.

various stages during loading and unloading are listed in Table 1. For WZ, the ratios  $cla$  and  $bla$  are 1.60 and 1.73, respectively. Throughout the transformation, the  $bla$  ratio remains at its initial value of 1.73 ( $\pm 0.02$ ), reflecting the symmetries of the loading and the lattice. On the other hand, upon transformation into BCT-4, the  $cla$  ratio changes to 1.7 and increases with further loading of the BCT-4 structured rod. The higher  $cla$  ratio reflects elastic stretching under the applied tensile stress in the  $c$  direction and the dimensional difference between WZ and BCT-4 structures. The transformation is complete at a strain of 8.5%, resulting in the formation of a BCT-4 structured nanorod. Further loading of the rod results in the elastic stretching of the BCT-4 structure ( $C \rightarrow D$ ) and culminates in the eventual failure at a strain of 16.9%.

The BCT-4 structure is analyzed using the radial distribution function (RDF). The RDF is a well-established technique for characterizing overall atomic structures and for evaluating average lattice parameters. It describes how atoms in a system are radially packed around each other by measuring the density of atoms in a spherical shell of radius  $r$  and thickness  $dr$  surrounding an atom in the structure. Specifically, the RDF is defined as

$$g(r) = \frac{n(r, r + dr)}{V_S} / \frac{N}{V}, \quad (9)$$

where  $n(r, r + dr)$  is the number of atoms in the spherical shell at distance  $r$  with thickness  $dr$ ,  $V_S = 4\pi r^2 dr$  is the volume of the spherical shell,  $N$  is the total number of atoms in the system and  $V$  is the volume of the structure. Fig. 4 shows the RDF profiles for the WZ structured rod after initial relaxation (corresponding to point A in Fig. 2) and the BCT-4 structured rod upon transformation completion (corresponding to point C in Fig. 2). For both structures, the first peak occurs approximately at 1.98 Å which corresponds to the Zn–O bond distance. Similarly, the second peaks for the two structures (corresponding to lattice constant  $a$ ) coincide, indicating that the two structures have the same lattice parameter along the initial  $[2\bar{1}\bar{1}0]$  orientation. Additionally, the ‘ $b$ ’ peaks for the WZ and BCT-4 structures also coincide, suggesting that the  $bla$  ratio remains constant during the transformation. However, the profiles (and hence the structures) are different from the

third peaks onward. The ‘ $c$ ’ peak for WZ at 5.20 Å shifts to 5.63 Å for BCT-4, causing the  $cla$  ratio to increase from 1.60 to 1.73. This change in  $c$  is consistent with the applied loading and the strain associated with the transformation into BCT-4.

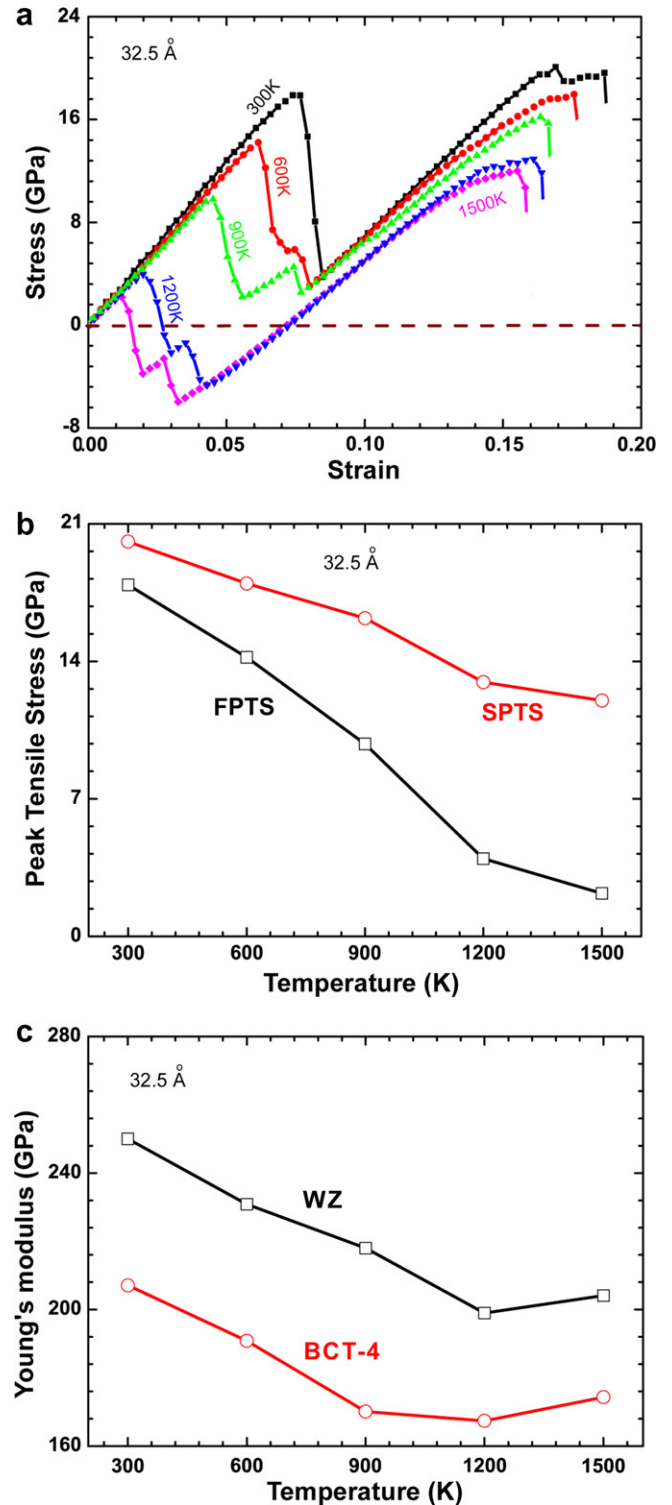


Fig. 6. Temperature dependence of response, (a) Stress–strain relations, (b) critical stress for transformation nucleation (FPTS) and failure strength (SPTS) and (c) elastic moduli of WZ and BCT-4.

Table 2

Critical stress for nucleation (FPTS), maximum tensile strength (SPTS), critical strains and elastic moduli of the nanorods at 300 K

Size (Å)	19.5	26.0	32.5	39.0	45.5
FPTS (GPa)	21.90	19.33	17.89	17.33	16.50
Strain at FPTS (%)	7.24	7.50	7.40	7.78	7.61
SPTS (GPa)	27.02	22.55	20.09	19.35	18.05
Strain at SPTS (%)	16.44	17.88	16.90	19.99	19.50
Elastic modulus of WZ (GPa)	299.49	271.05	250.02	238.19	227.51
Elastic modulus of BCT-4 (GPa)	269.29	219.50	207.14	183.43	166.86
Residual strain (%)	6.06	6.30	6.67	6.56	6.65

To analyze the stability of the BCT-4 structure, unloading is performed from various levels of strain along the loading path. Fig. 2 shows the unloading paths from points B and D which correspond to, respectively, the strains prior to transformation initiation (first peak tensile stress, FPTS) and eventual failure of the nanorod (second peak tensile stress, SPTS). The FPTS represents the critical stress required for the nucleation of the transformation. The path of unloading from B coincides with the loading path, confirming that the path A → B as indeed the elastic response of the WZ structured nanorod. Early states of unloading from D also results in the elastic recovery of the stretched the BCT-4 structure. However, unloading below the transformation completion strain (point C) does not result in a reverse transformation back into WZ. Instead, the nanorod retains the BCT-4 structure even when the stress is reduced to zero. The residual strain at F in Fig. 2 is 6.8% and reflects the dimensional difference between the unstressed WZ and BCT-4 structures in the [0001] direction.

*3.2. Size dependence*

The effect of lateral size on the response is also analyzed. Fig. 5a shows the stress–strain curves for nanorods of different sizes. The critical stress required for the nucleation of the transformation (FPTS) decreases by 25% from 21.90 to 16.50 GPa as the size increases from 19.5 to 45.5 Å (Fig. 5b). The failure stress (SPTS) is also size-dependent, decreasing 33% from 27.02 to 18.05 GPa over the same range of rod size. Detailed results are listed in Table 2. It is also observed that the stress–strain responses of smaller rods show an abrupt drop after the SPTS, indicating the occurrence of brittle failure, while the responses of larger rods show more gradual decrease in stress. This difference in behavior at different sizes is attributed to the higher degree of non-uniformity of deformation over the cross-section of rods with larger sizes. Note that the focus of the paper is the deformation behavior well before the initiation of failure at the SPTS. The failure behavior beginning at the SPTS can be the focus of a future analysis.

The elastic moduli of the nanorods (both WZ structured and BCT-4 structured) are higher than the corresponding value of 140 GPa [28,29] for bulk WZ and decrease as the size increases, as shown in Fig. 5c. The modulus of WZ structured rods decreases by 24% from 299.49 to 227.51 GPa as the lateral dimension is increased from 19.5 to 45.5 Å. On the other hand, the modulus of the BCT-4 struc-

tured rods decreases by 38% from 269.29 to 166.86 GPa over the same size range. The size dependence observed here can be explained by considering the state of stress in the nanorods. The high surface-to-volume ratios of the nanorods and the tensile surface-stress induce significant compressive stresses in the cores of rods. It has been shown that surface-stress-induced internal (compressive) stresses are inversely proportional to the lateral dimensions of nanostructures [3,7,30–32], effectively causing the size effect observed here. When cross-sectional dimensions are sufficiently large, surface-stress-induced compressive stresses are small and the surface effects are inconsequential. As a result, the material behavior approaches that of its bulk counterpart.

*3.3. Temperature dependence*

Temperature also has a significant effect on the critical stress required for transformation initiation and on the elastic responses of the WZ and BCT-4 structured rods. Fig. 6a shows the stress–strain curves associated for a 32.5 Å nanorod at 300, 600, 900, 1200 and 1500 K. The two linear elastic stages of deformation and the stress drop associated with the transformation are clear at all temperatures. A significant dependence of FPTS on temperature is observed. Specifically, as the temperature increases from 300 to 1500 K, the FPTS decreases 87.8% from 17.89 to 2.19 GPa, as shown in Table 3 and Fig. 6b. This decrease in transformation initiation stress is due to the enhanced ability of the nanorod to overcome the energy barrier at higher temperatures. At temperatures above 600 K, a transitional stage of linear response is observed. This stage of deformation corresponds to the stretching of a composite WZ + BCT-4 structure. The primary reason for the intermediate stage is that, at higher temperatures, the FPTS is lower and the strain energy stored in the WZ structured rod is not sufficient to drive the WZ → BCT-4 transformation for the whole rod. Instead, further stretching is required for the transformation to complete. Note that the deformation analyzed here is strain-controlled. At temperatures above 900 K, the FPTS is low enough such that there simply is not enough elongation of the rod at the initiation of the phase transformation (e.g., 1.98% and 1.21% for 1200 and 1500 K, respectively) to accommodate the dimensional increase associated with the WZ → BCT-4 transformation (approximately 6.8% for a 32.5 Å rod, see point F of Fig. 2). As a result, compressive stresses develop in the rods at such temperatures.

Table 3  
Critical stress for nucleation (FPTS), maximum tensile strength (SPTS), critical strains and elastic moduli of a 32.5 Å nanorod at different temperatures

Temperature (K)	300	600	900	1200	1500
FPTS (GPa)	17.89	14.20	9.79	3.96	2.19
Strain at FPTS (%)	7.40	6.14	4.52	1.98	1.21
SPTS (GPa)	20.09	17.97	16.20	12.94	12.00
Strain at SPTS (%)	16.90	17.57	16.36	16.11	15.52
Elastic modulus of WZ (GPa)	250.02	230.84	217.98	198.95	204.09
Elastic modulus of BCT-4 (GPa)	207.14	190.79	170.11	167.34	174.33

The enhanced mobility of atoms at higher temperatures promotes the formation of defects and cause significant thermal softening. As a result, a significant temperature dependence of the responses of the WZ and BCT-4 structures is also observed. Specifically, for 32.5 Å rod the elastic moduli of the WZ and BCT-4 structures decrease 18% and 16%, respectively, as temperature is increased from 300 to 1500 K (Fig. 6c). Over the same temperature range, the SPTS and the maximum elongation decrease by 40% and 8.17%, respectively, as shown in Fig. 6.

#### 4. Conclusion

The behavior of hexagonal ZnO nanorods with the [0001] growth direction, {0110}-facets and lateral dimensions between 19.5 and 45.5 Å is analyzed through atomistic simulations. A previously unknown structural transformation from the wurtzite structure to a body-centered-tetragonal structure with four-atom rings is observed. As a result of this transformation, the response of the nanorods to uniaxial tensile loading manifests in three stages, including (i) the elastic stretching of the WZ structure, (ii) a structural transformation from WZ to BCT-4 and (iii) the stretching of the BCT-4 structure. A significant dependence of deformation on rod size is observed. As the lateral dimension is increased from 19.5 to 45.5 Å, the elastic modulus values of the WZ and BCT-4 structured rods decrease by 24% and 38%, respectively, and the critical stress for transformation initiation decreases by 25%. This effect is attributed to surface-stress-induced internal compressive stresses in the nanorods. The behavior of the nanorods is also temperature-dependent, with the elastic moduli of the WZ and BCT-4 structures decreasing 18% and 16%, respectively, as temperature increases from 300 to 1500 K. The critical stress for transformation initiation shows the most pronounced temperature dependence, decreasing 87.8% over the same temperature range.

#### Acknowledgements

Support from the National Natural Science Foundation of China (NSFC) Grant Nos. 10772012, 10432050, and 10528205, from the Chinese Academy of Sciences (CAS) Innovation Program Grant No. KJCX2-YW-M04, and from the US National Science Foundation Grant No. CMS9984298 is gratefully acknowledged. Computations are performed in State Key Laboratory for Scientific and Engineering Computing of the CAS and at the NAVO and ASC MSRCs through AFOSR MURI no. D49620-02-1-0382.

#### References

- [1] Z.R. Dai, Z.W. Pan, Z.L. Wang, Gallium oxide nanoribbons and nanosheets, *J. Phys. Chem. B* 106 (2002) 902–904.
- [2] J. Diao, K. Gall, M.L. Dunn, Surface stress driven reorientation of gold nanowires, *Phys. Rev. B* 70 (2004) 075413.
- [3] W. Liang, M. Zhou, Pseudoelasticity of single crystalline Cu nanowires through reversible lattice reorientations, *J. Engr. Mater. Technol.* 127 (2005) 123–133.
- [4] W. Liang, M. Zhou, Atomistic simulations reveal shape memory of fcc metal nanowires, *Phys. Rev. B (Condens. Matter)* 73 (2006), 115409-115401-115411.
- [5] Z.W. Pan, Z.R. Dai, Z.L. Wang, Nanobelts of semiconducting oxides, *Science* 291 (2001) 1947–1949.
- [6] D.J. Binks. Computational modelling of zinc oxide and related oxide ceramics. PhD thesis, University of Surrey, Harwell, 1994.
- [7] A.J. Kulkarni, M. Zhou, Size-effects-dominated thermal and mechanical responses of zinc oxide nanobelts, *Acta Mech. Sinica* 22 (2006) 217–224.
- [8] A.J. Kulkarni, M. Zhou, Size-dependent thermal conductivity of zinc oxide nanobelts, *Appl. Phys. Lett.* 88 (2006), 141921-141921-141923.
- [9] A.J. Kulkarni, M. Zhou, F.J. Ke, Orientation and size dependence of the elastic properties of ZnO nanobelts, *Nanotechnology* 16 (2005) 2749–2756.
- [10] A.J. Kulkarni, M. Zhou, K. Sarasamak, S. Limpijumnong, Novel phase transformation in ZnO nanowires under tensile loading, *Phys. Rev. Lett.* 97 (2006), 105502-105501-105504.
- [11] Z.L. Wang, Zinc oxide nanostructures: growth, properties and applications, *J. Phys.: Condens. Matter* 16 (2004) R829–R858.
- [12] M.S. Arnold, P. Avouris, Z.W. Pan, Z.L. Wang, Field-effect transistors based on single semiconducting oxide nanobelts, *J. Phys. Chem.* 107 (2003) 659–663.
- [13] X.D. Bai, P.X. Gao, Z.L. Wang, W.G. Wang, Dual-mode resonance of individual ZnO nanobelts, *Appl. Phys. Lett.* 82 (2003) 4806–4808.
- [14] E. Comini, G. Faglia, G. Sberveglieri, Z.W. Pan, Z.L. Wang, Stable and highly sensitive gas sensors based on semiconducting oxide nanobelts, *Appl. Phys. Lett.* 81 (2002) 1869–1871.
- [15] W.L. Hughes, Z.L. Wang, Nanobelts as nanocantilevers, *Appl. Phys. Lett.* 82 (2003) 2886–2888.
- [16] Z.L. Wang, J. Song, Piezoelectric nanogenerators based on zinc oxide nanowire arrays, *Science* 312 (2006) 242–246.
- [17] A. Umar, B. Karunakaran, E.K. Suh, Y.B. Hahn, Structural and optical properties of single-crystalline ZnO nanorods grown on silicon by thermal evaporation, *Nanotechnology* 17 (2006) 4072.
- [18] A. Wei, X.W. Sun, C.X. Xu, Z.L. Dong, Y. Yang, S.T. Tan, W. Huang, Growth mechanism of tubular ZnO formed in aqueous solution, *Nanotechnology* 17 (2006) 1740.
- [19] J. Wang, A.J. Kulkarni, K. Sarasamak, S. Limpijumnong, F.J. Ke, M. Zhou, Molecular dynamics and density functional studies of a body-centered-tetragonal polymorph of ZnO, *Phys. Rev. B* 76 (2007) 172103.
- [20] D.J. Binks, R.W. Grimes, Incorporation of monovalent ions in ZnO and their influence on varistor degradation, *J. Am. Ceram. Soc.* 76 (1993) 2370–2372.
- [21] J.M. Haile, *Molecular Dynamics Simulation*, Wiley-Interscience, New York, 1997.
- [22] R.W. Grimes, D.J. Binks, A.B. Lidiard, The extent of zinc oxide solution in zinc chromate spinel, *Philos. Mag. A* 72 (1995) 651–668.
- [23] S. Melchionna, G. Ciccotti, B.L. Holian, Hoover NPT dynamics for systems varying in shape and size, *Mol. Phys.* 78 (1993) 533–544.
- [24] D. Spearot, K. Jacob, D.M. McDowell, Nucleation of dislocations from [001] bicrystal interfaces in aluminum, *Acta Mater.* 53 (2005) 3579–3589.
- [25] W. Smith, T.R. Forester, DL\_POLY is a molecular simulation routine written by W. Smith and T.R. Forester, copyright of CCLRC for the Central Laboratory of Research Councils, Daresbury Laboratory at Daresbury, Nr. Warrington, 1996.
- [26] M. Zhou, A new look at the atomic level virial stress: on continuum-molecular system equivalence, *Proc. R. Soc. London* 459 (2003) 2347–2392.
- [27] F. Claeysens, C.L. Freeman, N.L. Allan, Y. Sun, M.N.R. Ashfold, J.H. Harding, Growth of ZnO thin films—experiment and theory, *J. Mater. Chem.* 15 (2005) 139–148.

- [28] C.Q. Chen, Y. Shi, Y.S. Zhang, J. Zhu, Y.J. Yan, Size dependence of Young's modulus in ZnO nanowires, *Phys. Rev. Lett.* 96 (2006), 075505-075501-075504.
- [29] X.Y. Kong, Z.L. Wang, Spontaneous polarization-induced nano-helices, nanosprings, and nanorings of piezoelectric nanobelts, *Nano Lett.* 3 (2003) 1625–1631.
- [30] J. Diao, K. Gall, M.L. Dunn, Surface-stress-induced phase transformation in metal nanowires, *Nat. Mater.* 2 (2003) 656–660.
- [31] K. Gall, J. Diao, M.L. Dunn, The strength of gold nanowires, *Nano Lett.* 4 (2004) 2431–2436.
- [32] S. Sander, Surface stress: implications and measurements, *Curr. Opin. Solid State Mater. Sci.* 7 (2003) 51–57.